Cell Proliferation

Cell Prolif., 2013, **46**, 469–481 doi: 10.1111/cpr.12041

Oxygen consumption in T-47D cells immobilized in alginate

B. E. Larsen*, J. A. Sandvik†, J. Karlsen*, E. O. Pettersen† and J. E. Melvik‡

**School of Pharmacy, Universiy of Oslo, Oslo, 0316, Norway, †Department of Physics, University of Oslo, Oslo, 0316, Norway and ‡FMC Biopolymers AS, Sandvika, 1337, Norway*

Received 21 January 2013; revision accepted 6 April 2013

Abstract

Objectives: Encapsulation or entrapment of cells is increasingly being used in a wide variety of scientific studies for tissue engineering and development of novel medical devices. The effect on cell metabolism of such systems is, in general, not well characterized. In this work, a simple system for monitoring respiration of cells embedded in 3-D alginate cultures was characterized.

Materials and methods: T-47D cells were cultured in alginate gels. Oxygen concentration curves were recorded within cell-gel constructs using two different sensor systems, and cell viability and metabolic state were characterized using confocal microscopy and commercially available stains.

Results: At sufficient depth within constructs, recorded oxygen concentration curves were not significantly influenced by influx of oxygen through cell-gel layers and oxygen consumption rate could be calculated simply by dividing oxygen loss in the system per time, by the number of cells. This conclusion was supported by a 3-D numeric simulation. For the T-47D cells, the oxygen consumption rate was found to be 61 ± 6 fmol/cell/h, 3–4 times less than has previously been found for these cells, when grown exponentially in monolayer culture.

Conclusions: The experimental set-up presented here may be varied in multiple ways by changing the cell-gel construct 3-D microenvironment, easily allowing investigation of a variety of factors on cell respiration.

Correspondence: B. E. Larsen, School of Pharmacy, University of Oslo, P.O. Box 1068 Blindern, Oslo 0316, Norway. Tel.: +47 22 85 65 25; Fax: +47 22 85 44 02; E-mail: b.e.larsen@farmasi.uio.no

Introduction

Accurate description of the metabolism of cells entrapped in hydrogels is of great importance if bioartificial matrices are to be used as carrier substances for cells in various applications, such as in cancer research and regenerative medicine. Due to the protective effect of hypoxia on cells during treatment by irradiation (1,2), studies of oxygenation in 3-D tumour models may be important for development of better irradiation techniques. Such models have, for example, been used in the study of chemotherapeutic effectiveness and cancer cell colonization (3,4). In regenerative medicine and tissue engineering, oxygenation status of immobilized or encapsulated cells is also a crucial parameter in order to arrive at successful therapeutic applications (5).

Normal human tissues have wide variation between their cell densities, for example, 1.0–1.5 × 10^9 cells/cm³ in epidermal tissue (6), 2.4–3.0 × 10^8 cells/cm³ in the cerebral cortex (Heschl's gyrus) (7) and 0.4–52 × 10^6 cells/g in nasal septum cartilage (8). High cell densities demand high degrees of vascularization in most tissues and diffusion distances from capillaries, where oxygen tension is typically 30–40 mmHg (44–60 μM) (9), do not exceed a few μm in many tissues, such as brain and skeletal muscle (10,11). When it comes to survival of malignant cells, however, the limiting distance seems to be 50–250 μm (12).

In devices designed without a system that mimics natural vascularization or otherwise mediates perfusion, supply of nutrients, oxygen and signalling substances needs to take place by bulk diffusion (13). This is a crucial point in design of structures with cross-section greater than a few hundred micrometres. Importantly, diffusion-limited supply of oxygen can lead to hypoxia, a state in which cells significantly alter their metabolism and behaviour with consequences including increased glycolysis and reduced pericellular pH (14); unmitigated, it leads to impaired cell function or cell death (15).

Normal tissue oxygen tension varies from <3 mmHg (4 μM) to ~100 mmHg (~150 μM, alveoli) depending on

the tissue (16); this makes it difficult to define an exact, general threshold oxygen tension for hypoxia. HIF-1α is a key regulator of cell responses to hypoxia (17). It is constitutively expressed and degraded under normoxic conditions, but as oxygen is a necessary cofactor in its marking for degradation, it is activated when intracellular oxygen concentrations fall (18). It has been shown that it is activated *in vitro* in LS174Tr-cells (human colon adenocarcinoma cells) cultured in monolayers at oxygen concentrations of ~23 mmHg (32 μM) (19). Activation of HIF, however, precedes chronic and severe hypoxia, common in malignant cells; in the context of tumours, the limit for hypoxia is commonly set to 10–15 mmHg O_2 (14–22 μM) (20).

It is known that pericellular oxygen concentration limits intracellular consumption (21,22) at concentrations below approximately 0.1% (~1.5 μM) of ambient atmospheric pressure. For higher oxygen concentrations, the oxygen consumption rate (OCR) is generally not influenced by changes in oxygen concentration and cells are characterized by a baseline OCR. In general, pericellular oxygen concentration can be described as a function of (i) baseline OCR, (ii) number and density of cells, (iii) the system's physical characteristics (such as geometry, diffusivity) and (iv) the oxygen concentration in the system's supply (such as ambient atmosphere, perfusion chamber) (21,23). Observed, specific OCRs relate to intricacies of metabolic regulation, including factors such as metabolic history of the cells, specific cell–matrix interactions, current oxygenation and availability of other nutrients (24,25). In usual monolayer cultures, T-47D cells have been found to have an OCR of 177–227 fmol/cell/h (23).

The objective of this study was to develop a simple set-up for determination of OCR of cells entrapped in a hydrogel matrix, allowing careful studies to be carried out in a reproducible and efficient manner, thereby also providing reference for further studies of oxygen metabolism under 3-D cell culture conditions.

Materials and methods

Alginate

An internal gelling alginate-based system was used as 3-D cell matrix in the current work (26). Alginate gels were obtained by mixing alginate solution with a dispersion of calcium alginate particles, which initiated gelling as a result of calcium-ion exchange. All alginate materials were obtained from FMC Biopolymers/NovaMatrix (Sandvika, Norway). Low chain weight guluronate-rich (F_G = 67%) ultrapure sodium alginate (PRONONVA SLG-20 batch nos. 221105 and 130707/1), lyophilized and supplied in sterile vials, was dissolved in 4.6% w/w D-mannitol (Sigma, St Louis, MO, USA) in highly purified and sterile filtered water, to obtain a 2% w/w solution. Calcium alginate (PRONOVA Ca M, F_G = 46% batch nos. 701-05, 703-05 and BP-1108-01) was mixed with 4.6% w/w D-mannitol solution to 2% w/w dispersion, which was sterilized by autoclaving at 121 °C for 30 min. The particle size in the calcium alginate dispersion was between 45 and 75 μm and their calcium content was 9.6–10.2% (w/w).

Cell culture and extraction

T-47D cells (27) were cultured in 25 cm² cell culture flasks (Nunclon; Nunc Brand, Roskilde, Denmark), and recultured twice a week with change of culture medium late on day 2 or early day 3 of the 4-day growth period. Standard RPMI 1640 medium was used, supplemented with 130 IU/l human recombinant insulin (Sigma) 1% penicillin-streptomycin (Euroclone, Italy, art. No. ECB3055D) and 10% foetal bovine serum (FBS, Euroclone, Italy, art. No. ECS0180L), as described by Pettersen *et al.* (23). Cells were harvested for re-culture or for use in experiments by removing the growth medium, rinsing three times in 1.5 ml trypsin-EDTA solution (0.05% and 0.02%, respectively), and incubating cultures for 5 min at 37 °C in the residual trypsin solution. Cells were resuspended in fresh medium, and the number of extracted cells was calculated by counting 5–10 pre-determined plots in a haemocytometer or by using an automated cell counter (Countess; Invitrogen, Paisley, UK). After determining cell density, suspensions were spun down at 320 × g for 5 min and resuspended in medium to 4×10^6 cells/ml concentration. To avoid infection, all work was performed in laminar air flow benches using aseptic techniques.

Preparation of alginate biostructures

0.5 ml of both sodium alginate solution and calcium alginate was separately dispensed in two 1 ml syringes joined by a three-way connector; until dispensed, calcium alginate dispersion was kept in suspension using a magnetic stirrer. Cells were suspended in 100 μl medium and transferred to syringes containing calcium alginate dispersion by carefully emptying the micropipette containing the suspension at the nozzle of the syringe, while retracting its piston. The two gelling components were transferred through the connector between the syringes 10 times in a timed and rehearsed manner to initialize gelling. The three-way connector was opened and mixed contents emptied into standard test tubes (acid-cleaned borosilicate glass; Pyrex, Lowell, MA, USA) 75 mm in length and 10 mm internal diameter.

This biostructure was left for 5 min to allow initial gelling to occur, then subsequently covered with 2.5 ml RPMI 1640 medium.

Cell viability assessment

Five hundred micrometres sections of prepared biostructures were taken at day 0, 1, 3, 7 and 9 using a vibratome (Microm HM 650 V, Waldorf, Germany), operated at blade speed 0.5 mm/s, amplitude of 1.2 mm and blade oscillation frequency of 70 Hz, with nominal slice thickness of 500 μm. Sections prepared in this manner were transferred to 35 mm Petri dishes and incubated with calcein AM and ethidium homodimer (Invitrogen) in Hank's balanced salts (Sigma-Aldrich, St. Louis, MO, H2387-10XK) for 15 min at 37 °C.

Specimens were examined by confocal microscopy (Nikon, Tokyo, Japan) using 488 and 543 nm excitation laser light; emission light was measured at 515–530 nm (calcein, viable cells) and 605–675 nm (ethidium homodimer, dead cells); the software alternated pairs of excitation and detection frequencies to exclude cross-talk. Final images were averages of 3 scans. Depth of sections assessed was ~300–500 μm, yielding stacks of approximately 60–100 slices. Images were pre-processed and stacked in.ics format using Nikon EasyZ software (Nikon). These files were loaded into ImageJ (National Institutes of Health, Bethesda, MD, USA) and analysed using an Object Counter software plug-in (3D Object Counter; Fabrice Cordelires, Institut Curie, Orsay, France and Jonathan Jackson, UCL Institute of Neurology, London, UK. 2007)). A custom Matlab (ver R2010a; The Mathworks, Natick, MA, USA) script was used to detect double-stained cells, which were counted as non-viable.

Pimonidazole hypoxia assay

Alginate biostructures as described above were prepared using sodium alginate, which had been dissolved in 4.55% aqueous D-mannitol solution containing 200 μM pimonidazole (pimo) (Hypoxyprobe, Burlington, MA, USA) and incubated under the same conditions. Gel sections were prepared as described above, but incubated for 25 min in a solution containing FITC-marked murine anti-pimonidazole IgG (Hypoxyprobe) and ethidium homodimer (Invitrogen) at concentrations recommended by the manufacturers. Sections were then examined using confocal microscopy as described above, with emission light at 515–530 nm from FITC-conjugated anti-pimonidazole murine antibodies and 605–675 nm (ethidium homodimer, dead cells). After this, the same samples were incubated with live/dead staining solution as described above, and re-imaged. Calcein fluorescence was far stronger than anti-pimo mab-FITC fluorescence, and a neutral density filter (ND4) was used to dim the 488 nm laser when re-imaging with calcein-AM. Without calcein-AM present, this filter, together with volume thresholds in the counting software, prevented anti-pimo mab-FITC fluorescent cells from being counted. Proportions of pimonidazole-stained cells were calculated on the basis of proportion of ethidium homodimer-stained cells according to eqn (1), where N_{pimo} is the number of pimo-stained cells, $N_{\mathrm{ethidium(c)}}$ the number of ethidium-stained cells found when samples were re-imaged with calcein-AM present, $N_{\mathrm{ethidium(p)}}$ the number of ethidium-stained cells in the first imaging run with pimo and $N_{\mathrm{TOT(c)}}$ the total number of cells found in the second imaging run with ethidium homodimer and calcein-AM.

$$p_{\mathrm{pimo}} = \frac{N_{\mathrm{pimo}} \cdot N_{\mathrm{ethidium(c)}}}{N_{\mathrm{ethidium(p)}} \cdot N_{\mathrm{TOT(c)}}} \quad (1)$$

Oxygen measurements

Oxygen concentrations listed in this work, where not given in μM units, were converted to μM units for ease of comparison. Conversion was made under the assumption that cited measurements were made at 37 °C, 101.3 kPa, 5% CO_2 and a colligative effect equal to 4 salinity.

During O_2-measurements, the set-up described in Fig. 1 was either kept in a Forma Scientific (Marietta, OH, USA) incubator (model 3862) using HEPA-filtered atmospheric air with 5% CO_2 and 80–85% relative humidity, or in a Ruskinn™ Invivo 400 hypoxic workstation (Ruskinn Technology Ltd., Bridgend, UK) operated at 19.0% O_2 and 5% CO_2 with relative humidity of ~80–100%.

A syringe-mounted needle-type fibre-optic oxygen microsensor, with a diameter of 140 μm, manufactured by PreSens GmbH (Regensburg, Germany) was used with a PreSens Microx TX3 oxygen meter. Oxygen concentration was continuously logged at a predefined, stationary position, inside the biostructures. Also, a Clarke-type OX-10 oxygen microsensor connected to a picoammeter and mounted on a micromanipulator , both connected to a desktop computer with integrated software measurement logging and motor control (all manufactured by UniSense, Arhus, Denmark) was used to measure oxygen concentration as a function of time and microsensor position in the system. Here, the manufacturer specifies that the sensor has a defined OCR of 4×10^{-13} to 5×10^{-12} mol O_2/h, which is negligible in the current context. Both sensors were calibrated against a 3% aqueous solution of $NaSO_3$ (Fluka Analytical/ Sigma-Aldrich, St. Louis, MO, USA) (0 μM O_2)

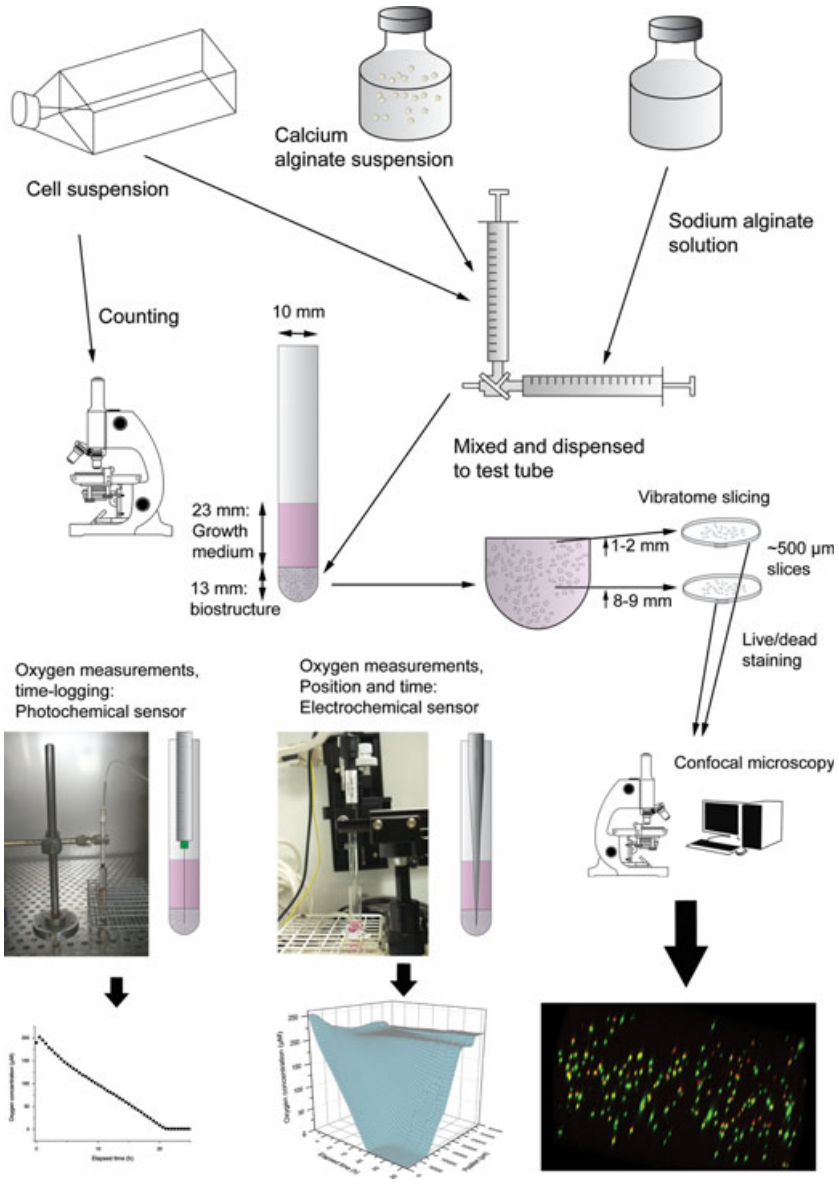

Figure 1. Flow chart showing sample preparation, system dimensions, data acquisition methods and representative data. The geometric dimensions of the set-up were standardized as a consequence of using identical quantities of growth medium, alginate gel and identical test tubes between experiments.

and water vapour saturated ambient air (210 µM O_2 at 37 °C, 101.3 kPa). Calibration was performed either at 37 °C (both) or at ambient temperature (22–25 °C) using in-built direct temperature compensation features (PreSens sensor only).

Calculation of oxygen consumption rates

When calculating OCRs, taking data points early in experiments, together with a relatively long medium column separating biostructure from incubator atmosphere, meant that oxygen influx through diffusion had little impact (see below). For each oxygen concentration measurement series, the continuous derivative function was calculated numerically. Equation (2) was used to calculate OCR per cell:

$$R = \frac{\Delta n}{\Delta t \cdot N_{\mathrm{m}}} = \frac{(C_1 - C_2) \cdot V_{\mathrm{m}}}{(t_1 - t_2) d_{\mathrm{c}} V_{\mathrm{m}}} \qquad (2)$$

Here R is the OCR per cell, C_1 and C_2 are oxygen concentrations measured at t_1 and t_2, and $N_{\mathrm{m}} = d_{\mathrm{c}} \cdot V_{\mathrm{m}}$ is the number of metabolizing cells in the system. V_{m} is the measurement volume, while d_{c} is the density of metabolizing cells in the gel, calculated as in eqn (3). The change in the quantity of oxygen present, Δn, is the product of measurement volume and concentration

change. As the measurement volume enters into both the nominator and the denominator, it is not needed for the final calculation.

$$d_c = \frac{S \cdot N_0}{V_{gel}} \quad (3)$$

Here, S denotes viability as estimated by counting confocal microscopy image stacks recorded from live/dead-stained gel sections taken from specimens immediately after preparation. N_0 denotes number of cells originally added to the specimen, estimated by counting samples of cell suspension in haemocytometers, and V_{gel} is the volume of hydrogel used. It differs from V_m by the volume of gel left in the dead volume of the syringes and three-way connector.

The following assumptions were made without compensating for uncertainty: (i) distribution of cells in the matrix did not influence concentration measurements. (ii) efficiency of all stains was 100%.

Computer analyses and statistics

A diffusion model was used to calculate theoretical time and depth oxygen consumption profiles. For this, Matlab R2010a (The Mathworks) was used to create simple logic circuits to define system boundaries and to calculate concentration profile values by means of an iterative algorithm. For simplicity, a uniform oxygen concentration of 200 μM was set for all points at $t = 0$. The algorithm was set to determine oxygen concentration at 1-min intervals and in 500 μm thick discrete sections. In the profile shown (Fig. 4), OCR was set to 0.167 μM per 1 min interval, and 82% of the gradient spanning the two points immediately above and below the point being evaluated was assumed to be equilibrated per time interval. The equilibration rate was calculated from a diffusion constant determined using published equations (28).

Origin 8.5 (OriginLab, Northampton, MA, USA) was used for all statistical analyses and numerical evaluation of derivative curves. All estimates are given as mean ± standard error, unless otherwise stated.

Results

System characterization

Oxygen concentration was recorded as function of time and microsensor position, using a micromanipulator-mounted Clark-type microsensor. In this experiment, controller software was programmed to position the sensor tip 1 cm below culture medium surface, within the medium column, between measurement series. To minimize oxygen gradient perturbation in the medium column, each measurement cycle begun with the sensor being moved to its lowermost position within the gel. To avoid placing the very fragile glass microsensor at risk, the lowest point programmed in measurement cycles was usually approximately 4–5 mm above the test tube bottom. From there, measurements were recorded in 500 μm upward steps until the medium surface was reached, with a 5 s equilibration period preceding a 5 s measurement period at each step. The assumption was that larger sensor movements carried a greater risk of inducing convective currents in the medium column and that such perturbations would be offset during the period when the sensor moved in small steps, allowing the gradient to reform. A waiting period of 500–1000 s between measurement cycles was also programmed, each measurement cycle thus lasting approximately 30 min. In all experiments, gel puncture caused by the sensor's penetration apparently resealed as the sensor was withdrawn.

Oxygen initially present in the biostructure containing approximately 2.5×10^5 viable cells/ml (that is, at positions from 0 to about 7000 μm on the surface plot in Fig. 2) was consumed within 24 h, and oxygen concentration remained relatively uniform in deeper layers of the structure at each time point. At time points close to the beginning of the experiment, oxygen concentration within the system was measured to be higher than theoretically possible at steady state in the incubator. This is believed to be a result of the variable conditions under which the biostructure, consisting of cells embedded in the alginate gel, was prepared; ambient temperature was below 37 °C and there was no CO_2 in the gas phase. This is believed to explain higher oxygen concentration in the system and was, for practical reasons, difficult to avoid.

As initially available oxygen stores within the biostructure were gradually consumed by cell respiration, an oxygen gradient was established through the lower parts of the medium (Fig. 2). In some experiments using a slightly different set up, with cell density increased to around 8×10^5 cells/ml, the volume that was oxygen depleted, with oxygen concentration below the sensitivity level of the oxygen sensor (<1 μM), extended beyond the biostructure, into the lower regions of the culture medium column (Fig. 3).

Oxygen diffusion throughout the system was also computer simulated to allow comparison of experimental data with diffusion theory. The numerical model (Fig. 4) and experimental data shared similar features: in the oxygen-consuming region, a concentration gradient was found, which over time shifted downwards. Furthermore, due to high oxygen consumption by the cells, oxygen concentration in the lowermost parts was not

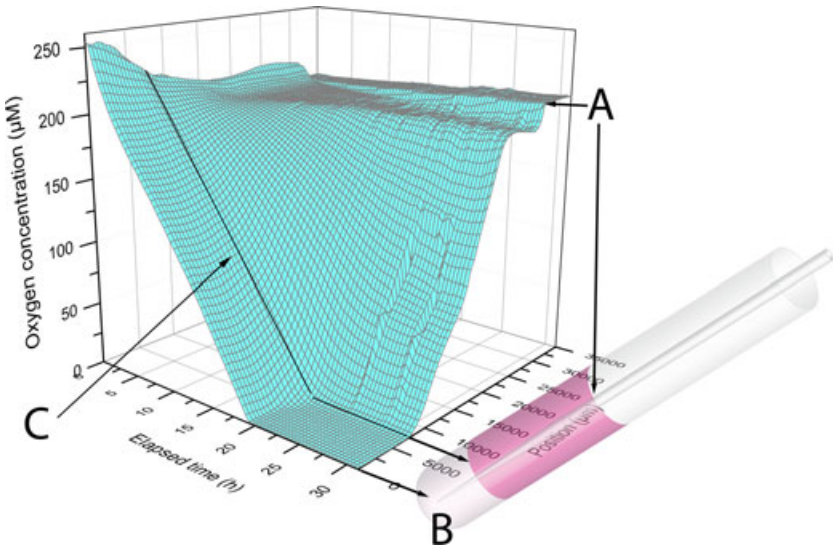

Figure 2. 3D surface plot showing the oxygen concentration as a function of elapsed time and microsensor (Clark-type) position. Black lines and arrows show approximate corresponding positions in the gel/medium system. Each line on the surface represents a given time series (parallel to position axis) or position series (parallel to time axis). A denotes the medium surface, where surface tension around the sensor tip results in a narrow plateau. B is the approximate bottom position of the microsensor. C denotes the biostructuregrowth medium border. The oxygen concentration was recorded in 500 µm upward steps and the alginate biostructure was seeded with approximately 2.3×10^5 viable cells. The gel and medium volumes were 0.9 and 2.5 ml respectively.

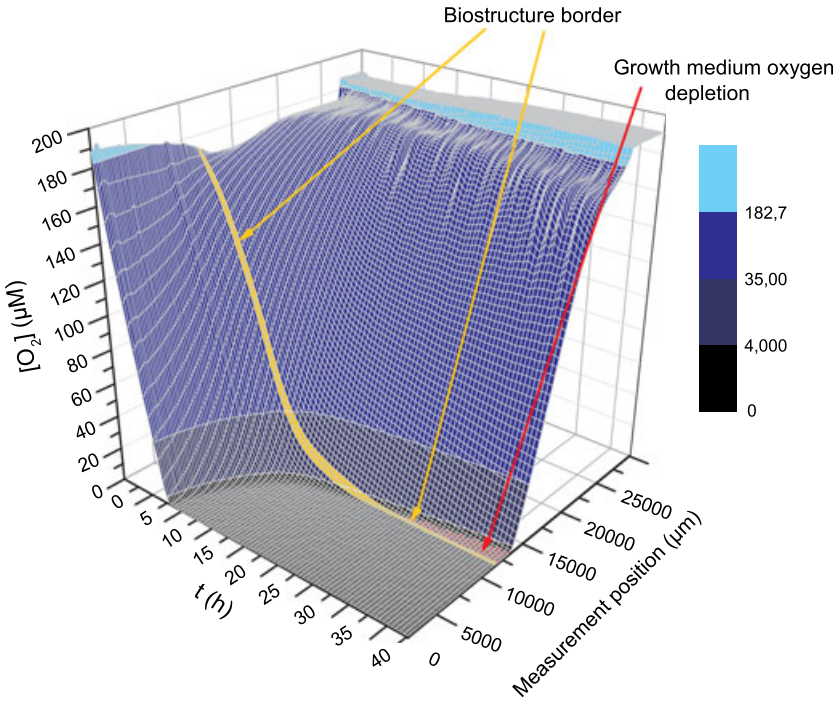

Figure 3. 3D surface plot similar to Fig. 2 with slightly different experimental parameters: the oxygen concentration was recorded in 200 µm upward steps and the alginate biostructure was seeded with approximately 8×10^5 cells. Colour map: Oxygen concentrations corresponding to ambient air or above (light cyan), below ambient air and normoxic concentrations (blue), hypoxic concentrations (dark blue), and severely hypoxic concentrations (black). Arrows point to the biostructure-growth medium interface (yellow) and an area that denotes oxygen depletion in the growth medium above the biostructure.

influenced by diffusion through the construct. As oxygen was consumed by the cells, its concentration approached zero also in lower parts of the medium reservoir (this effect appears stronger in Fig. 3 due to high cell number) and both lower and upper inflexion points of the gradient shifted slowly upwards.

Hypoxia and viability

Cell viability was assessed separately in sections retrieved from within 1–2 mm of the biostructure-medium interface and in sections 8–9 mm from this limit at different time points. Results, as seen in Figs 5 and 6, demonstrate higher loss in viability of cells situated farther away from the gel–medium interface, over time. Initial differences in viability seen between the two gel sections is believed to be a result of variations in sample handling. The overall tendency was therefore that within less than 24 h, depending on cell density, oxygen initially present within the gel was consumed, while cell viability remained unchanged. Over the subsequent days, cells in the oxygen-deprived region lost their membrane integrity at a rate dependent on their position relative to the medium reservoir.

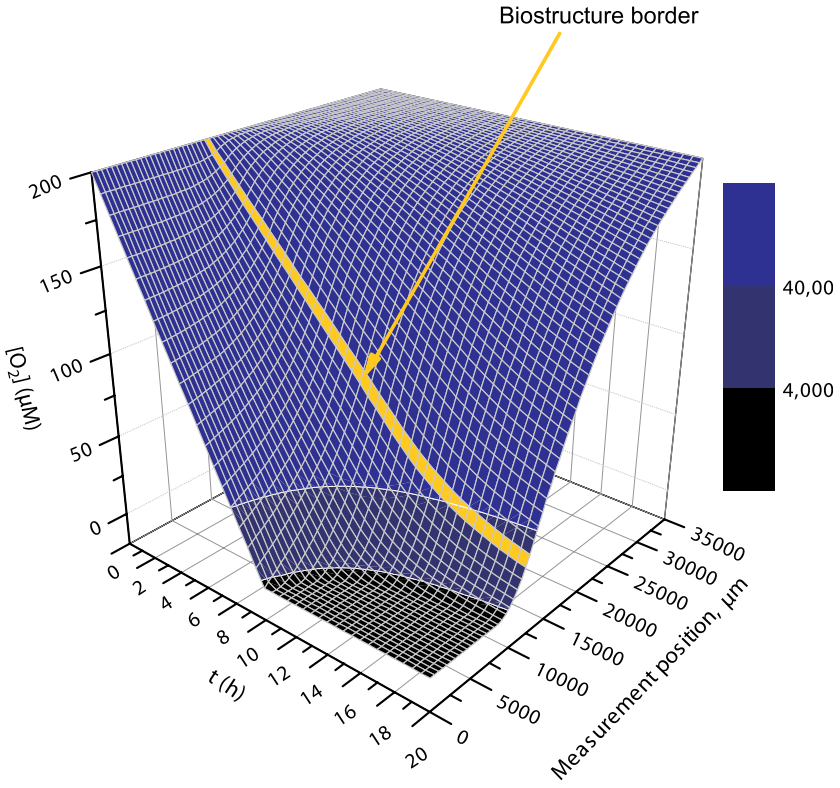

Figure 4. 3D surface plot showing simulated oxygen concentrations as a function of time and measurement position. The oxygen concentration at the medium surface ($x = 0$) and at $t = 0$ was set to 200 μM and the oxygen consumption rate to 10 μM/h. Diffusion was calculated iteratively from $x = 35\,000$ to $x = 0$ (corresponding to the micrometre scale of the experiments) in 500 μm steps, assuming that 82% of the gradient between two points separated by 500 μm would be equilibrated per minute (see main text for details). Colour map: Oxygen concentrations corresponding to normoxic concentrations (blue), hypoxic concentrations (dark blue), and severely hypoxic concentrations (black). The yellow line signifies the simulated biostructure-growth medium boundary.

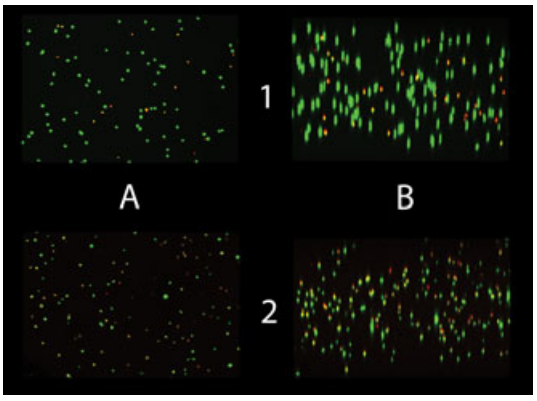

Figure 5. Representative lateral and vertical views of confocal image stacks obtained from live/dead-stained gel slices. Both images are taken from the bioconstruct interior, at day 0 in the upper row, and at day 7 in the lower. The images in column A are vertical views, in column B lateral views. Lateral views are software rendered from about 100 individual vertical-view images. Green objects are stained by calcein AM, red by ethidium homodimer. Yellow objects represent structures that are stained by both ethidium and calcein. The main contribution to the observed reduction in viability over time came from an increased fraction of cells stained with both markers.

As seen in Fig. 6, increasing proportions of cells stained with both calcein-AM and ethidium homodimer, indicated membrane disturbances that nonetheless allowed cytoplasmic esterases to remain active. Development of hypoxia in the pericellular environment was indicated by increased staining with FITC-labelled antibodies against pimonidazole moieties (Fig. 6). Several immunostained images, particularly those recorded on days 1 and 3, could not be assessed by the Object Counter software plug-in due to high levels of background fluorescence and were counted manually. Data also indicated correlation between pimonidazole/FITC-mab and ethidium homodimer staining over time (results not shown).

Rates of oxygen consumption

To determine more precisely OCRs of the cells within the construct, a set up with a stationary optical oxygen sensor was used. As mentioned above, although some care was taken to limit temperature variations in samples during preparation, reduced temperature of the cell-gel mixture during mixing and initial gelling had an effect on oxygen measurements. As can be seen in Fig. 7, oxygen concentration measured initially was higher than the theoretical maximum of dissolved oxygen at 37 °C. The oxygen sensing equipment used has an in-built temperature sensor and software temperature compensation, but the temperature sensor was considerably larger than the oxygen sensors. It was therefore judged that it would disturb measurements and thermostat temperature of the

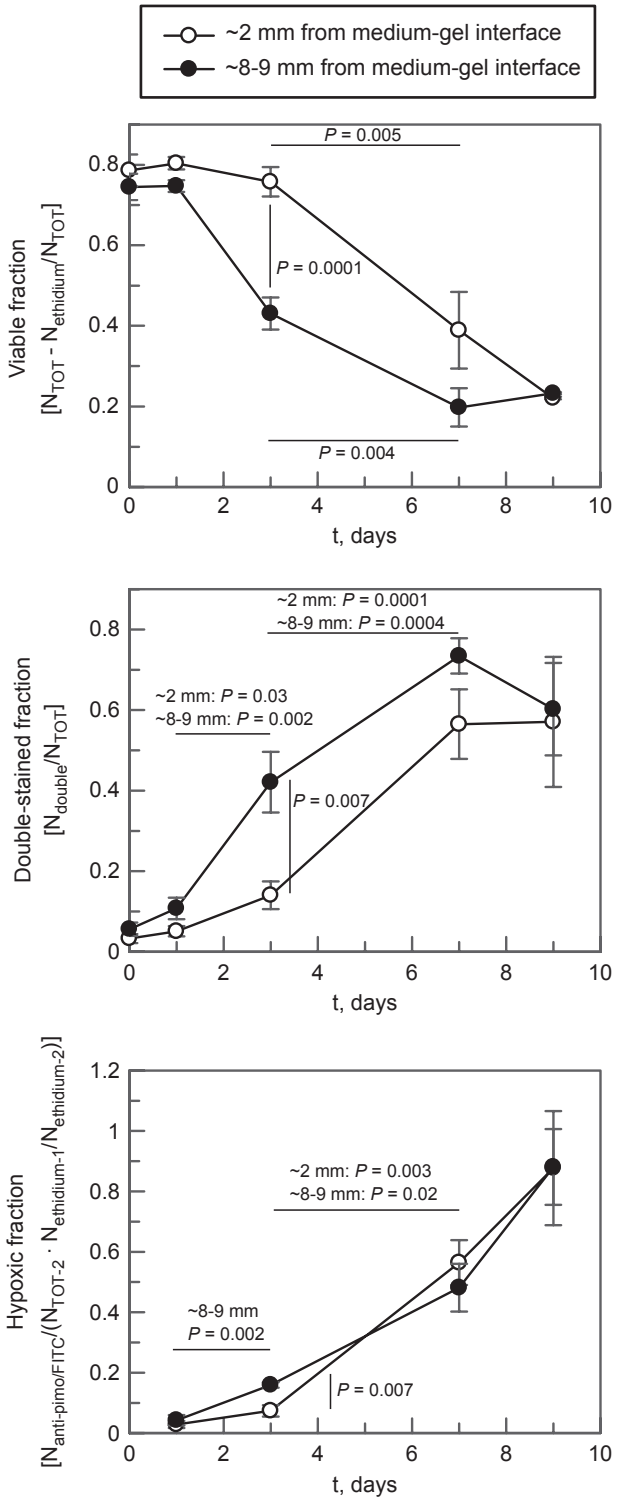

Figure 6. Upper panel: Viability as a function of time, as determined by calcein AM and ethidium homodimer staining using confocal microscopy. The examined sections were taken 1–2 and 8–9 mm from the biostructure-growth medium interface. Error bars denote standard error of the mean calculated from three to six parallels (n = 3 for days 0 and 9, n = 6 for days 1–7). The thick lines link with corresponding P-values demonstrating significant differences in viability (Student's t-test). **Middle panel:** The proportion of cells staining for both ethidium homodimer and calcein AM as a function of time. The fraction of double-stained cells increased markedly over the first 7 days. The lines link with corresponding P-values demonstrating significant differences. Error bars denote standard error of the mean calculated for three to six parallels (taken from the same experiment as the upper panel). **Lower panel:** The fraction of cells stained by anti-pimonidazole FITC-marked murine antibodies (pimo-mab). The fraction was calculated by first staining with pimo-mab and ethidium homodimer (ethidium-1), examining the sample by confocal microscopy before re-staining the same sample with calcein AM and ethidium homodimer (ethidium-2). The number of ethidium homodimer-stained cells was then determined and used as a reference (TOT-2). Statistically significant differences between adjacent data points are shown with P-values.

incubators was used as temperature reference instead. Separate measurements confirmed that temperature within the incubators was stable at 37.0 °C and at all times was within 36.4–37.6 °C.

To minimize the influence of unequilibrated temperature and pCO_2 on calculated change in oxygen concentration (ΔC), and to allow cells to metabolically stabilize within the system, the first data points in the oxygen concentration time series were discarded; only points recorded after 2.5 h had elapsed were used for calculation of OCRs. At this time, oxygen concentration in the biostructure interior was within the theoretically possible concentration range for incubation conditions at 37 °C (28). Depending on cell density, time needed to reach oxygen concentrations below sensor sensitivity threshold within the biostructure interior varied from 4 to 22 h. Estimates of time-dependent OCR up to this point were calculated from continuous derivative plots and assessments of cell density (Fig. 8).

Mean OCR reported here is based on experiments where nominal cell count added to gel mixture was 400 000. Mean density of metabolizing cells, corrected for syringe ejection volume and viability, was $2.37 \times 10^5 \pm 0.07 \times 10^5$/ml. Data points used to calculate oxygen concentration changes were recorded in the bioconstruct interior 2.5–5 h into the experiments and mean gel volume was $9.2 \times 10 \pm 0.3 \times 10$/ml. Based on these estimates, the OCR was found to be 61 ± 6 fmol/cell/h. If the next 12 oxygen concentration data points were included (up to 11 h, when the first parallel had almost depleted initial oxygen stores); mean OCR was 51 ± 4 fmol/cell/h.

Discussion

Two simple experimental systems (Fig. 1), using either a micromanipulator-controlled sensor system or a stationary sensor embedded in the gel, allowed for careful

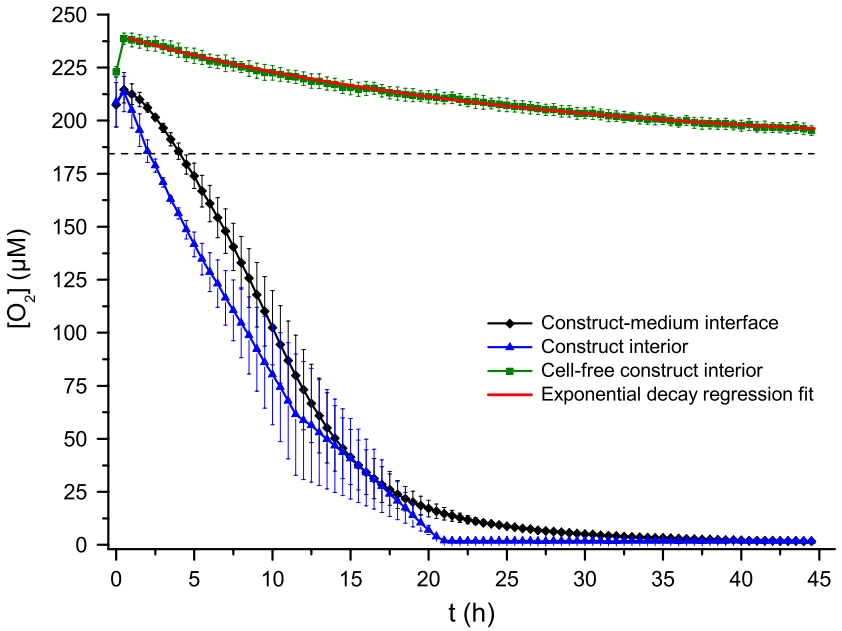

Figure 7. Oxygen concentration as a function of time close to the biostructure-growth medium interface and in the biostructure interior recorded using an optical sensor. The theoretical oxygen concentration in water at 37 °C, 101.3 kPa, 5% CO_2 and a mix of solutes corresponding to a salinity of 4 equals 182.7 µmol/l and is shown as a dashed line. The mean oxygen concentration curve recorded in a cell-free system was fitted to an exponential decay function which converged at 187.1 µmol/l (red line). Error bars denote standard error of the mean calculated for three parallels.

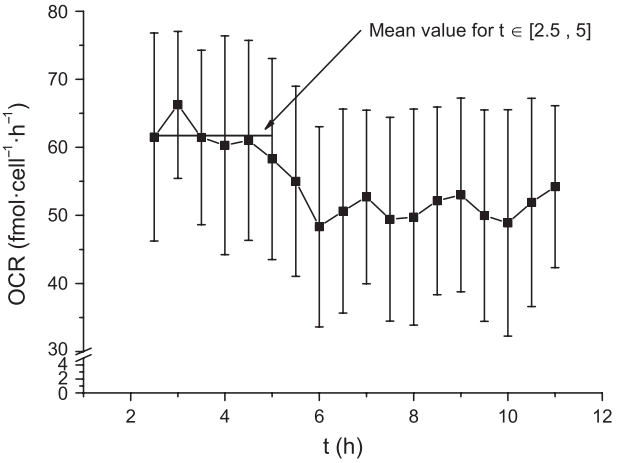

Figure 8. Oxygen consumption rate as a function of time, based on the derivative of the concentration curve recorded in the bioconstruct interior (Fig. 7) and the number of viable cells (Fig. 6). The mean oxygen consumption rate was calculated by using data points between 2.5 and 5 h (red horizontal bar). This time frame was chosen in order to exclude contribution by temperature effects and diffusion of oxygen from the growth medium into the gel. Error bars denote standard error of the mean calculated from three parallels.

determination of oxygen concentration as a function of cell position and time. As borosilicate glass is impenetrable to oxygen, and the biostructure filled the entire width of the test tubes, this was considered to exclude any radial oxygen gradient. Some irregularities were nonetheless evident in the data. In Figs 2 and 3, an effect of the meniscus around the sensor tip can be clearly seen as a steep, short gradient just below the surface of the culture medium. These observations were assumed to be a result of surface evaporation either leading to a slightly higher salinity or lower temperature (29). Furthermore, oxygen concentrations above the theoretical equilibrium in the CO_2-incubator, particularly at the beginning of the experiments, were believed to be a result of differences in temperature and gas composition occurring during sample preparation, and of incubator environment. It could not be ruled out that movement of the micromanipulator resulted in some convection through the medium column and it was therefore decided to use a stationary optical sensor to determine OCR of entrapped cells. The two methods, however, produced very similar results of oxygen consumption within the gel centre (results not shown).

Rapid depletion of available oxygen stores was also expected, based on previously published reports using established cell lines (30,31). In contrast, cells of primary cultures frequently downregulate metabolism at concentration thresholds higher than those observed here (32,33), making it possible for some cell types, for example chondrocytes, to endure enforced hypoxia for 7 days or longer (34,35). It has been demonstrated that short-term hypoxia does not necessarily compromise viability and proliferation in a microcapsular system (30) or monolayer cultures (36).

At sufficient distance from the gel–growth medium interface, oxygen concentration appeared to fall linearly with time until initial oxygen stores were depleted, with little or no contribution from oxygen diffusing into the gel. This was also observed in the computer-simulated data (Figs 2, 3, 4 and 7). Cell OCR was calculated from

mean derivative of oxygen-time plots of three parallel experiments (Fig. 8), and based on the former observations, it was assumed that for cells in the biostructure interior, contribution from the influx of oxygen was negligible. The observations were in accordance with an oxygen gradient in the vertical direction only. However, non-linear fall in oxygen concentration in the cell-seeded gel was observed near the gel–culture medium interface (Fig. 7). Comparison of experiments with computer simulation suggested that near this border, influx of oxygen took place by diffusion, and increased as oxygen concentration fell, due to an increased oxygen gradient towards the medium (Figs 2, 3, 4 and 7).

As consumption of oxygen within the cell-alginate construct was higher than supply from the medium *via* diffusion, oxygen concentration within the hydrogel fell below the sensors' sensitivity threshold (1–2 μM) (cf. Figs 2, 3 and 6). Below this level, cell respiration would necessarily be reduced (21). It seems reasonable to assume that after this has occurred, reduced oxygen consumption is established as a result of consumption by a remaining fraction of cells still maintaining aerobic metabolism. Under this assumption, influx of oxygen by diffusion through the medium gradient would be in the order of $1.15–1.30 \times 10^{-11}$ mol/h, somewhat less than one tenth oxygen consumption in the system as a whole during the normoxic phase. In this respect, it is interesting to note that cell viability apparently stabilized at about 20% over the last two days (7 and 9) of the experiments.

Cells were uniformly dispersed throughout the cell-gel bioconstruct (Fig 5). Due to the slow rate of diffusion of oxygen in water and the distance to the medium-biostructure interface, measurements recorded using the optical sensor within the biostructure interior, 8–9 mm from the gel–growth medium interface, should largely be unaffected by oxygen diffusing into the biostructure; more than half the biostructure volume was above this position. Cells situated in the upper volume would presumably consume any oxygen diffusing downwards from the oxygenated medium column. Relative influence of oxygen influx from the environment would also necessarily be reduced if cell density was increased, giving a steeper gradient (Figs 2 and 3).

Pimonidazole is a well-established exogenous indicator of chronic hypoxia (37), and has been shown to bind to proteins in severely hypoxic cells, at oxygen concentrations below around 14 μM (11 mmHg) (38,39), when the most common endogenous indicator, HIF, is no longer active (40). In this study, it was found that acute hypoxia, as shown by pimonidazole binding, was negligible in the first 24 h after experiments begun, but increased as they progressed, reaching up to 80% of all cells by day 9, when only 20% of all cells were still membrane-intact (Fig. 6). Thus, plasma membrane disruption apparently still allowed some esterase activity, as collocation of calcein AM and ethidium homodimer continued to increase for some days in the hypoxic environment. To some extent, increase in ethidium staining also seemed to follow an increase in pimonidazole incorporation (Fig. 6).

Onset of cell death, occurring after 1–2 days, was more rapid in the bioconstruct interior than close to the gel–medium interface (Figs 5 and 6); depletion of available oxygen stores was quite similar at the two positions (Fig. 7). It therefore seems likely that some diffusion of oxygen at concentrations below the sensors' limits, and possibly also better availability of other nutrients, led to prolonged higher viability for cells at the medium interface. Apparent delay in incorporation of pimonidazole (Fig. 6) may also support this hypothesis. In the experiments, it was found that cell density at the gel–medium interface did not vary significantly between day 0 and day 7 ($P = 0.41$, $df = 4$) (results not shown), and cell proliferation therefore seems unlikely.

Based on our experiments, the most reliable calculation of the cells' OCR was obtained from the initial linear component of the oxygen concentration curves recorded within the gel interior, after allowing the system to stabilize (Figs 7 and 8). Average OCR for the T-47D cells calculated on the basis of data recorded between 2.5 and 5 h after onset of the experiments was 61 ± 6 fmol/cell/h. Considerably higher OCR of 177–227 fmol/cell/h has previously been measured by our group for T-47D cells grown exponentially in monolayer culture (23), using the same strain of T-47D cells, same culture and harvesting protocols and operating under the same group-wide culture plan, ensuring a comparable passage number.

The lower oxygen concentration limit for full respiration rate of T-47D cells has previously been found to be 0.13% (41), in the order of 1.3 μM. This cell line was established under ambient air atmospheric conditions (27) and displays deficient regulation of oxygen metabolism compared to normal cells.

Viable cell fraction after entrapment in the cell-gel construct, as indicated by cell calcein AM and ethidium homodimer staining (Fig. 6), was in relatively good agreement with previously published data for cells immobilized in hydrogels (42,43). Recent studies have shown that use of cross-linked alginate gels, such as those used in the present work, has a cytoprotective effect when cells are subjected to ejection through syringes, leading to viability ranges closely corresponding to those presented here, ~70% (43). Mechanism of cell death was not investigated in the present study, but presence of cell debris from ruptured and dying cells may perhaps have relevance in a clinical setting.

Many researchers have demonstrated that when cells are entrapped in 3-D gel environments, proximity to culture medium is of importance for survival and function of the cells (31–33,44–48). Some reports have shown that viability in nutrient-limited systems does not necessarily follow a smoothly decreasing tendency (49). An increase in the fraction of cells staining for both calcein AM and ethidium homodimer (Fig. 7) indicates that in the present system cells underwent increasing membrane destabilization, suggesting that other pathways than apoptosis constituted the main routes of cell death (50). A similar phenomenon has been reported by other workers (51), although in their case geometry of the system was quite different and double-staining diminished with time.

In a study of alginate-immobilized Vero cells [a line derived from kidney epithelial cells of African green monkeys (52)], maximal population growth was found after 4 days (49), while oxidative stress increased significantly with time, presumably due to limited nutrient supply; after 7 days or so, this led to significant loss of viability. As in our case, their experimental set-up was likely to cause hypoxia and nutrient deprivation due to diffusion-limited supply. Supply of serum growth factors was presumably higher than in the experiments shown here, as culture medium was supplied directly into the matrix, albeit at a low rate. In a later study, it was shown that the Vero cell line proliferated only at a very low rate in an oxygen-restricted alginate environment, as opposed to in alginate beads (53). Other workers have shown that extensive cell population growth in microcapsules follows after a certain lag period, although under quite different physical conditions (54). T-47D cells used here would normally be growing exponentially in monolayer culture. Some possible explanations may be that they failed to proliferate within the alginate scaffold due to lack of essential growth factors or nutrients, lack of attachment to the surrounding matrix and constraints by rigidity of the gel network. It has, however, been demonstrated that T-47D cells are able to proliferate without anchorage and singularly dispersed at densities similar to those used here, with colony formation taking 10–14 days (55).

Cell–matrix interactions have previously been reported to affect OCRs of bovine chondrocytes immobilized in agarose compared to collagen gels; Guaccio *et al.* argue that RGD peptide may influence OCR, as soluble RGD peptides were found to elicit higher respiration rates in RGD-free agarose scaffolds (56). On a general note, T-47D cells also require cytokines and growth factors from serum to be successfully cultured *in vitro* (57). Some of these may have their diffusion impeded by an alginate gel network. Also, in the present experiments, no binding motifs existed in the gel. Diffusion-limited supply of compounds such as growth factors and other important metabolic factors for *in vitro*-immobilized cells, has previously been reported by Griffith *et al.*(58) and suggested by Heywood *et al.*(45). In the present work, a small amount of serum was included in the cell suspension, but not nearly as much as under ordinary culture conditions (~1% versus 10%). It may be suggested as a hypothesis that the lower respiration rate of T-47D cells entrapped in a 3-D alginate scaffold compared to monolayer culture may be related to a variety of factors including loss of attachment, or reduced supply of nutrients or metabolic factors, leading to downregulation or possibly cessation of cell proliferation. Further investigation will be needed to clarify this.

We believe that the experimental set-up presented here allows further adaptation to investigate specific changes in 3-D culture environments and the influence of a variety of factors on cell respiration.

In conclusion, a basic set-up for assessment of cell OCRs in an alginate 3-D environment has been established. Data obtained are consistent with a fixed OCR for T47D cells entrapped within the gel, until hypoxic conditions were reached. Calculated OCR was found to be significantly lower than previously found for T-47D cells grown in exponential monolayer culture.

Acknowledgements

The authors thank FMC Biopolymers AS for the kind supply of alginate materials and use of laboratory facilities. Research in this article was also partially funded through the EUROXY and METOXIA projects under the European Union Framework Programmes for Research and Technological Development.

References

1 Ranalli NJ, Evans SM, Judy KD (2009) Hypoxia in brain tumors. *Neurosurg. Quart.* **19**, 1–12.
2 Svensson H, Möller TR (2003) Developments in radiotherapy. *Acta Oncol.* **42**, 430–442.
3 Kievit FM, Florczyk SJ, Leung MC, Veiseh O, Park JO, Disis ML *et al.* (2010) Chitosan-alginate 3D scaffolds as a mimic of the glioma tumor microenvironment. *Biomaterials* **31**, 5903–5910.
4 Burdett E, Kasper FK, Mikos AG, Ludwig JA (2010) Engineering tumors: a tissue engineering perspective in cancer biology. *Tissue Eng. Part B Rev.* **16**, 351–359.
5 Ikada Y (2006) Challenges in tissue engineering. *J. R. Soc. Interface* **3**, 589–601.
6 Bauer J, Bahmer FA, Worl J, Neuhuber W, Schuler G, Fartasch M (2001) A strikingly constant ratio exists between Langerhans cells and other epidermal cells in human skin. A stereologic study using

the optical disector method and the confocal laser scanning microscope. *J. Invest. Dermatol.* **116**, 313–318.
7 Cotter D, Mackay D, Frangou S, Hudson L, Landau S (2004) Cell density and cortical thickness in Heschl's gyrus in schizophrenia, major depression and bipolar disorder. *Br. J. Psychiat.* **185**, 258–259.
8 Homicz MR, McGowan KB, Lottman LM, Beh G, Sah RL, Watson D (2003) A compositional analysis of human nasal septal cartilage. *Arch. Facial Plast. Surg.* **5**, 53–58.
9 Wang W, Vadgama P (2004) O_2 microsensors for minimally invasive tissue monitoring. *J. R. Soc. Interface* **1**, 109–117.
10 Jensen JH, Lu H, Inglese M (2006) Microvessel density estimation in the human brain by means of dynamic contrast-enhanced echo-planar imaging. *Magn. Reson. Med.* **56**, 1145–1150.
11 McGuire BJ, Secomb TW (2003) Estimation of capillary density in human skeletal muscle based on maximal oxygen consumption rates. *Am. J. Physiol. Heart Circ. Physiol.* **285**, 2382–2391.
12 Sutherland RM (1988) Cell and environment interactions in tumor microregions: the multicell spheroid model. *Science* **240**, 177–184.
13 Colton CK (1996) Engineering challenges in cell-encapsulation technology. *Trends Biotechnol.* **14**, 158–162.
14 Alberti KGMM (1977) The biochemical consequences of hypoxia. *J. Clin. Pathol. Suppl.* **11**, 14–20.
15 Sowter HM, Ratcliffe PJ, Watson P, Greenberg AH, Harris AL (2001) HIF-1-dependent regulation of hypoxic induction of the cell death factors BNIP3 and NIX in human tumors. *Cancer Res.* **61**, 6669–6673.
16 Porwol T, Ehleben W, Brand V, Acker H (2001) Tissue oxygen sensor function of NADPH oxidase isoforms, an unusual cytochrome aa3 and reactive oxygen species. *Respir. Physiol.* **128**, 331–348.
17 Greer SN, Metcalf JL, Wang Y, Ohh M (2012) The updated biology of hypoxia-inducible factor. *EMBO J.* **31**, 2448–2460.
18 Maxwell PH, Wiesener MS, Chang G-W, Clifford SC, Vaux EC, Cockman ME *et al.* (1999) The tumour suppressor protein VHL targets hypoxia-inducible factors for oxygen-dependent proteolysis. *Nature* **399**, 271–275.
19 Dayan F, Roux D, Brahimi-Horn MC, Pouyssegur J, Mazure NM (2006) The oxygen sensor factor-inhibiting hypoxia-inducible factor-1 controls expression of distinct genes through the bifunctional transcriptional character of hypoxia-inducible factor-1α. *Cancer Res.* **66**, 3688–3698.
20 Hou H, Dong R, Li H, Williams B, Lariviere JP, Hekmatyar SK *et al.* (2012) Dynamic changes in oxygenation of intracranial tumor and contralateral brain during tumor growth and carbogen breathing: a multisite EPR oximetry with implantable resonators. *J. Magn. Reson.* **214**, 22–28.
21 Boag JW (1970) Cell respiration as a function of oxygen tension. *Int. J. Radiat. Biol. Relat. Stud. Phys. Chem. Med.* **18**, 475–478.
22 Froese G (1962) The respiration of ascites tumour cells at low oxygen concentrations. *Biochim. Biophys. Acta* **57**, 509–519.
23 Pettersen EO, Larsen LH, Ramsing NB, Ebbesen P (2005) Pericellular oxygen depletion during ordinary tissue culturing, measured with oxygen microsensors. *Cell Prolif.* **38**, 257–267.
24 Amellem O, Stokke T, Sandvik JA, Pettersen EO (1996) The retinoblastoma gene product is reversibly dephosphorylated and bound in the nucleus in S and G(2) phases during hypoxic stress. *Exp. Cell Res.* **227**, 106–115.
25 Sander EA, Nauman EA (2010) Effects of reduced oxygen and glucose levels on ocular cells in vitro: implications for tissue models. *Cells Tissues Organs.* **191**, 141–151.
26 Kristiansen A, Andersen T, Melvik JE (2007) Cells, gels and alginates. *Eur. Biopharm. Rev.* **Spring**, 34–38.
27 Keydar I, Chen L, Karby S, Weiss FR, Delarea J, Radu M *et al.* (1979) Establishment and characterization of a cell-line of human-breast carcinoma origin. *Eur. J. Cancer* **15**, 659–670.
28 Garcia HE, Gordon LI (1992) Oxygen solubility in seawater – better fitting equations. *Limnol. Oceanogr.* **37**, 1307–1312.
29 Gundersen JK, Ramsing NB, Glud RN (1998) Predicting the signal of O_2 microsensors from physical dimensions, temperature, salinity, and O_2 concentration. *Limnol. Oceanogr.* **43**, 1932–1937.
30 Papas KK, Long RC, Sambanis A, Constantinidis I (1999) Development of a bioartificial pancreas: I. long-term propagation and basal and induced secretion from entrapped betaTC3 cell cultures. *Biotechnol. Bioeng.* **66**, 219–230.
31 Volkmer E, Drosse I, Otto S, Stangelmayer A, Stengele M, Kallukalam BC *et al.* (2008) Hypoxia in static and dynamic 3D culture systems for tissue engineering of bone. *Tissue Eng.* **14**, 1331–1340.
32 Malda J, Rouwkema J, Martens DE, Le Comte EP, Kooy FK, Tramper J *et al.* (2004) Oxygen gradients in tissue-engineered PEGT/PBT cartilaginous constructs: measurement and modeling. *Biotechnol. Bioeng.* **86**, 9–18.
33 Radisic M, Malda J, Epping E, Geng W, Langer R, Vunjak-Novakovic G (2005) Oxygen gradients correlate with cell density and cell viability in engineered cardiac tissue. *Biotechnol. Bioeng.* **93**, 332–343.
34 Grimshaw MJ, Mason RM (2000) Bovine articular chondrocyte function in vitro depends upon oxygen tension. *Osteoarthr. Cartil.* **8**, 386–392.
35 Schneider N, Lejeune JP, Deby C, Deby-Dupont GP, Serteyn D (2004) Viability of equine articular chondrocytes in alginate beads exposed to different oxygen tensions. *Vet J.* **168**, 167–173.
36 Amellem Ø, Stokke T, Sandvik JA, Smedshammer L, Pettersen EO (1997) Hypoxia-induced apoptosis in human cells with normal p53 status and function, without any alteration in the nuclear protein level. *Exp. Cell Res.* **232**, 361–370.
37 Kizaka-Kondoh S, Konse-Nagasawa H (2009) Significance of nitroimidazole compounds and hypoxia-inducible factor-1 for imaging tumor hypoxia. *Cancer Sci.* **100**, 1366–1373.
38 Arteel GE, Thurman RG, Yates JM, Raleigh JA (1995) Evidence that hypoxia markers detect oxygen gradients in liver: pimonidazole and retrograde perfusion of rat-liver. *Br. J. Cancer* **72**, 889–895.
39 Arteel GE, Thurman RG, Raleigh JA (1998) Reductive metabolism of the hypoxia marker pimonidazole is regulated by oxygen tension independent of the pyridine nucleotide redox state. *Eur. J. Biochem.* **253**, 743–750.
40 Sobhanifar S, Aquino-Parsons C, Stanbridge EJ, Olive P (2005) Reduced expression of hypoxia-inducible factor-1 alpha in perinecrotic regions of solid tumors. *Cancer Res.* **65**, 7259–7266.
41 Amellem O, Sandvik JA, Stokke T, Pettersen EO (1998) The retinoblastoma protein-associated cell cycle arrest in S-phase under moderate hypoxia is disrupted in cells expressing HPV18 E7 oncoprotein. *Br. J. Cancer* **77**, 862–872.
42 Kong HJ, Smith MK, Mooney DJ (2003) Designing alginate hydrogels to maintain viability of immobilized cells. *Biomaterials* **24**, 4023–4029.
43 Aguado B, Mulyasasmita W, Su J, Lampe KJ, Heilshorn S (2011) Improving viability of stem cells during syringe needle flow through the design of hydrogel cell carriers. *Tissue Eng. Part A* **18**, 806–815.
44 Boubriak OA, Urban JPG, Cui ZF (2006) Monitoring of metabolite gradients in tissue-engineered constructs. *J. R. Soc. Interface* **3**, 637–648.
45 Heywood HK, Sembi PK, Lee DA, Bader DL (2004) Cellular utilization determines viability and matrix distribution profiles in chondrocyte-seeded alginate constructs. *Tissue Eng.* **10**, 1467–1479.

46 Chung CA, Chen CW, Chen CP, Tseng CS (2007) Enhancement of cell growth in tissue-engineering constructs under direct perfusion: modeling and simulation. *Biotechnol. Bioeng.* **97**, 1603–1616.
47 Lewis MC, MacArthur BD, Malda J, Pettet G, Please CP (2005) Heterogeneous proliferation within engineered cartilaginous tissue: the role of oxygen tension. *Biotechnol. Bioeng.* **91**, 607–615.
48 Cheema U, Brown RA, Alp B, MacRobert AJ (2008) Spatially defined oxygen gradients and vascular endothelial growth factor expression in an engineered 3D cell model. *Cell. Mol. Life Sci.* **65**, 177–186.
49 Kintzios S, Marinopoulou I, Moschopoulou G, Mangana O, Nomikou K, Endo K *et al.* (2006) Development of a novel, multi-analyte biosensor system for assaying cell division: identification of cell proliferation/death precursor events. *Biosens. Bioelectron.* **21**, 1365–1373.
50 Gatti R, Belletti S, Orlandini G, Bussolati O, Dall'Asta V, Gazzola GC (1998) Comparison of annexin V and Calcein-AM as early vital markers of apoptosis in adherent cells by confocal laser microscopy. *J. Histochem. Cytochem.* **46**, 895–900.
51 Galateanu B, Dimonie D, Vasile E, Nae S, Cimpean A, Costache M (2012) Layer-shaped alginate hydrogels enhance the biological performance of human adipose-derived stem cells. *BMC Biotechnol.* **12**, 35.
52 Yasumura Y, Kawatika Y (1963) Studies on SV40 in tissue culture-preliminary step for cancer research in vitro. *Nippon Rinsho* **21**, 1201–1215.
53 Kintzios S, Yiakoumetis I, Moschopoulou G, Mangana O, Nomikou K, Simonian A (2007) Differential effect of the shape of calcium alginate matrices on the physiology of immobilized neuroblastoma N2a and Vero cells: a comparative study. *Biosens. Bioelectron.* **23**, 543–548.
54 Stabler C, Wilks K, Sambanis A, Constantinidis I (2001) The effects of alginate composition on encapsulated bTC3 cells. *Biomaterials* **22**, 1301–1310.
55 Tseng MT, Safa AR (1983) Light, fluorescent, and electron microscopic analysis of cultured breast tumor cells (T-47D) treated with 9,10-anthracenedicarboxaldehyde Bis[(4,5-dihydro-1H-imidazol-2-yl)hydrazone] dihydrochloride. *Cancer Res.*. **43**, 5910–5914.
56 Guaccio A, Borselli C, Oliviero O, Netti PA (2008) Oxygen consumption of chondrocytes in agarose and collagen gels: a comparative analysis. *Biomaterials* **29**, 1484–1493.
57 Shi YH, Wang YX, Bingle L, Gong LH, Heng WJ, Li Y *et al.* (2005) In vitro study of HIF-1 activation and VEGF release by bFGF in the T47D breast cancer cell line under normoxic conditions: involvement of PI-3K/Akt and MEK1/ERK pathways. *J. Pathol.* **205**, 530–536.
58 Griffith CK, Miller C, Sainson R, Calvert JW, Jeon NL, Hughes CCW *et al.* (2005) Diffusion limits of an in vitro thick prevascularized tissue. *Tissue Eng.* **11**, 257–266.